A Corticothalamic Switch: Controlling the Thalamus with Dynamic Synapses

Highlights

- The influence of layer 6 corticothalamic neurons on the thalamus is dynamic

- The nature of corticothalamic actions depends critically on firing frequency

- Low frequencies mainly suppress thalamic excitability; high frequencies enhance it

- Synaptic dynamics mediate the changes in sign of corticothalamic influence

Authors

Shane R. Crandall, Scott J. Cruikshank, Barry W. Connors

Correspondence

bc@brown.edu

In Brief

The thalamus regulates sensory throughput to the neocortex, but the neocortex is also a major source of input to the thalamus. Crandall et al. reveal the dynamic mechanisms of cortical control over thalamic gating, providing a fresh framework for understanding this top-down pathway.

A Corticothalamic Switch: Controlling the Thalamus with Dynamic Synapses

Shane R. Crandall,[1,2] Scott J. Cruikshank,[1,2] and Barry W. Connors[1,*]

[1]Department of Neuroscience, Brown University, 185 Meeting Street, Box G-LN, Providence, RI 02912, USA
[2]Co-first author
*Correspondence: bc@brown.edu
http://dx.doi.org/10.1016/j.neuron.2015.03.040

SUMMARY

Corticothalamic neurons provide massive input to the thalamus. This top-down projection may allow the cortex to regulate sensory processing by modulating the excitability of thalamic cells. Layer 6 corticothalamic neurons monosynaptically excite thalamocortical cells, but also indirectly inhibit them by driving inhibitory cells of the thalamic reticular nucleus. Whether corticothalamic activity generally suppresses or excites the thalamus remains unclear. Here we show that the corticothalamic influence is dynamic, with the excitatory-inhibitory balance shifting in an activity-dependent fashion. During low-frequency activity, corticothalamic effects are mainly suppressive, whereas higher-frequency activity (even a short bout of gamma frequency oscillations) converts the corticothalamic influence to enhancement. The mechanism of this switching depends on distinct forms of short-term synaptic plasticity across multiple corticothalamic circuit components. Our results reveal an activity-dependent mechanism by which corticothalamic neurons can bidirectionally switch the excitability and sensory throughput of the thalamus, possibly to meet changing behavioral demands.

INTRODUCTION

Virtually all sensory information enters the neocortex by way of the thalamus. The transfer of sensory signals from the periphery to the cortex is not simply a one-to-one relay but a dynamic process involving reciprocal communication between the cortex and thalamus. An intriguing feature of thalamocortical (TC) and corticothalamic (CT) systems is that descending CT axons greatly outnumber ascending TC axons by about 10:1 (Deschênes et al., 1998; Sherman and Koch, 1986). Moreover, CT axons provide the predominant synaptic input to the sensory thalamus, accounting for 30%–44% of all synapses that TC cells receive (Erişir et al., 1997; Liu et al., 1995; Van Horn et al., 2000). This curious organization suggests that the cortex must have a strong influence on thalamic activities and, thereby, its own sensory input.

Given the potential power of the CT pathway, a great deal of in vivo work has addressed its functions during sensory processing (for reviews, see Briggs and Usrey, 2008; Cudeiro and Sillito, 2006). It is generally thought that the cortex influences thalamic throughput by modulating the excitability and spiking behavior of TC cells. However, the scale and even the sign of that modulation vary widely across studies, and there is no consensus about the mechanisms controlling these differences.

This uncertainty may relate to CT circuit complexity. CT cells of layer 6 (L6) are a direct source of excitatory input to TC cells (Bourassa et al., 1995; Golshani et al., 2001; Lam and Sherman, 2010; Scharfman et al., 1990), but they also indirectly inhibit them by exciting GABAergic cells in the thalamic reticular nucleus (TRN) (Figure 1A; Cox et al., 1997; Golshani et al., 2001; Kim et al., 1997; Lam and Sherman, 2010). Consequently, the sign of CT modulation (enhancement or suppression) will depend on the interactions and balance between disynaptic feedforward inhibition and monosynaptic excitation. The cells and pathways mediating this balance are closely adjacent to one another, involve both recurrent and reciprocal connectivity, and lie deep within the brain (Deschênes et al., 1998). This has made it difficult to access and isolate critical CT structures and processes using conventional in vivo approaches. As an alternative, we turned to optogenetics and an in vitro preparation of the mouse somatosensory forebrain that preserves the essential CT circuitry of the system (Agmon and Connors, 1991; Cruikshank et al., 2010; Kao and Coulter, 1997). This preparation strips away most of the extrinsic circuitry present in fully intact brains, simplifying and facilitating the targeted mechanistic investigation of each cell type and synapse in the CT processing chain. Using this approach, we revealed an integrated dynamic picture of top-down CT actions on thalamic excitability. Our results provide essential building blocks for understanding cortical control of thalamic sensory processing and perhaps mechanisms underlying processes such as directed attention and perception.

RESULTS

To explore cortical influences on thalamic processing, we applied optogenetic control strategies (Figures 1A–1C) (Cruikshank et al., 2010; Jurgens et al., 2012; Olsen et al., 2012; Paz et al., 2011). Using a Cre-Lox system, we conditionally expressed the light-sensitive cation channel channelrhodopsin-2 (ChR2) in L6 CT cells in the vibrissal region of the mouse somatosensory cortex (barrel cortex, *Ntsr1-Cre* mice) (Bortone et al., 2014; Gong et al., 2007; Kim et al., 2014; Mease et al., 2014;
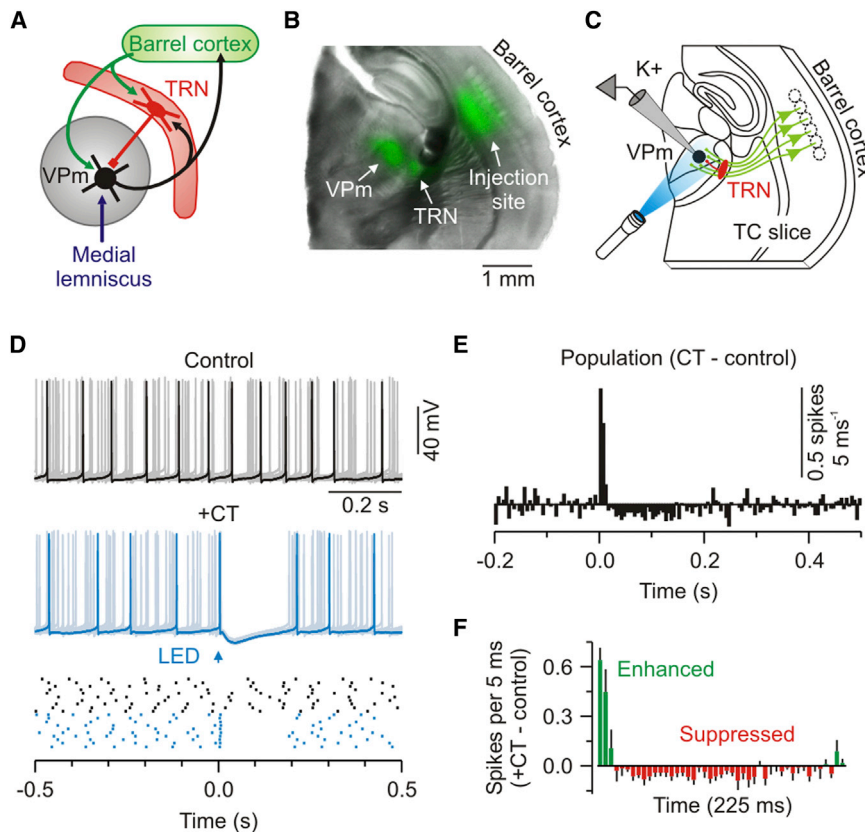
Figure 1. Low-Frequency CT Stimuli Modulate VPm Excitability

(A) Schematic of the principal pathway for whisker-related sensory processing in the rodent forebrain.

(B) Image of a live TC slice (300 μm) from an *Ntsr1-Cre* mouse injected in the barrel cortex with an adeno-associated virus (AAV) driving Cre-dependent ChR2-EYFP expression in L6 CT cells. Shown is an overlay of EYFP (green) and bright field (gray). See also Figure S1.

(C) Schematic of the recording configuration. Shown is the optical stimulation of ChR2-expressing CT axons (green) and whole-cell recording (K+ solution) from a ChR2-negative VPm cell (black).

(D) Top: control activity from a VPm neuron during injection of depolarizing current (overlay of 10 sweeps). Center: the same cell and conditions except addition of CT stimulation (arrow, 1 ms flash; trials repeated at 0.1 Hz). Bottom: raster plot of the cell's spiking. Control (black) and +CT (blue) trials are plotted as clustered groups for displays but were interleaved during testing.

(E) Population peristimulus time histogram (PSTH, 5-ms bins) plotting the difference in spike rates for CT versus control trials (n = 9 cells from 5 mice).

(F) Population PSTH showing the first 225 ms after CT stimulation.

(D–F) Cells were injected with 30–110 pA to produce ~12-Hz baseline firing rates. CT stimulus intensities were 2× threshold for IPSPs (mean = 3.02 mW). Data are represented as mean ± SEM. See also Figure S2.

Olsen et al., 2012). L6 CT cells expressed ChR2-enhanced yellow fluorescent protein (EYFP) in their somata, dendrites, axons, and terminals within the thalamus (Figure 1B; Figure S1). This allowed for selective optical control of CT projections in the thalamus (Figure 1C).

Functional CT Modulation of the VPm

We first tested how CT inputs modulate excitability and processing in the ventral posterior medial nucleus (VPm, the core vibrissal division of the somatosensory thalamus). VPm cells were injected with positive current to produce a sustained discharge (~12 Hz) comparable with tonic spiking during awake states (Hirsch et al., 1983; Steriade et al., 1993), and then the effects of optical CT stimuli on that spiking were measured. L6 neurons, including CT cells, in vivo are often reported to have very low spiking rates (Kwegyir-Afful and Simons, 2009; Landry and Dykes, 1985; Lee et al., 2008; O'Connor et al., 2010; Swadlow, 1989). Therefore, we elected to initially stimulate the CT pathway at 0.1 Hz. Such CT stimulation caused robust biphasic modulation of VPm spiking (Figure 1D). There was an initial transient (~15 ms) increase in spike rates, followed consistently by a much longer period of suppression (>100 ms; Figures 1E and 1F). This confirms that cortical input can exert powerful influences on the thalamus and indicates that low-frequency CT activity primarily suppresses thalamic cell excitability.

The medial lemniscus (ML) is the major ascending sensory pathway carrying whisker-related information into the thalamus (Diamond et al., 2008). To determine whether CT-mediated changes in VPm excitability affect the thalamic transfer of sensory signals, we paired optical CT activation with electrical stimulation of ML axons. When single ML axons were stimulated in isolation using a minimal stimulation protocol, responses in VPm cells were fast and powerful and displayed little variability (ML-evoked excitatory postsynaptic currents (EPSCs), 2.5 ± 0.5 nA when held in voltage clamp at −89 mV; n = 9 cells from 7 mice; Figures S2A–S2E; Castro-Alamancos, 2002; Miyata, 2007). However, when ML afferents were stimulated shortly after CT stimulation, there was significant modulation of VPm responses (Figures S2F–S2H). The sign of the modulation (enhancement or suppression) was strongly dependent on the CT-ML interval. CT stimulation caused an early phase (<25 ms) of enhancement and a later phase (~100 ms) of suppression, consistent with the biphasic effects on excitability as described (Figures 1D–1F).

Although CT activity has been reported to be sparse under many conditions (Kwegyir-Afful and Simons, 2009; Landry and Dykes, 1985; Lee et al., 2008; Swadlow, 1989), studies have shown that L6 neurons, including CT cells, can fire for sustained periods and at moderately high rates (~10 Hz or more) when alert animals are presented with appropriate sensory stimuli or during spontaneous gamma-band oscillations (Y. Bereshpolova et al., 2013, Soc. Neurosci., abstract; Briggs and Usrey, 2009a, b; O'Connor et al., 2010; Swadlow and Weyand, 1987; Zhou et al., 2010). To characterize the functional consequences of
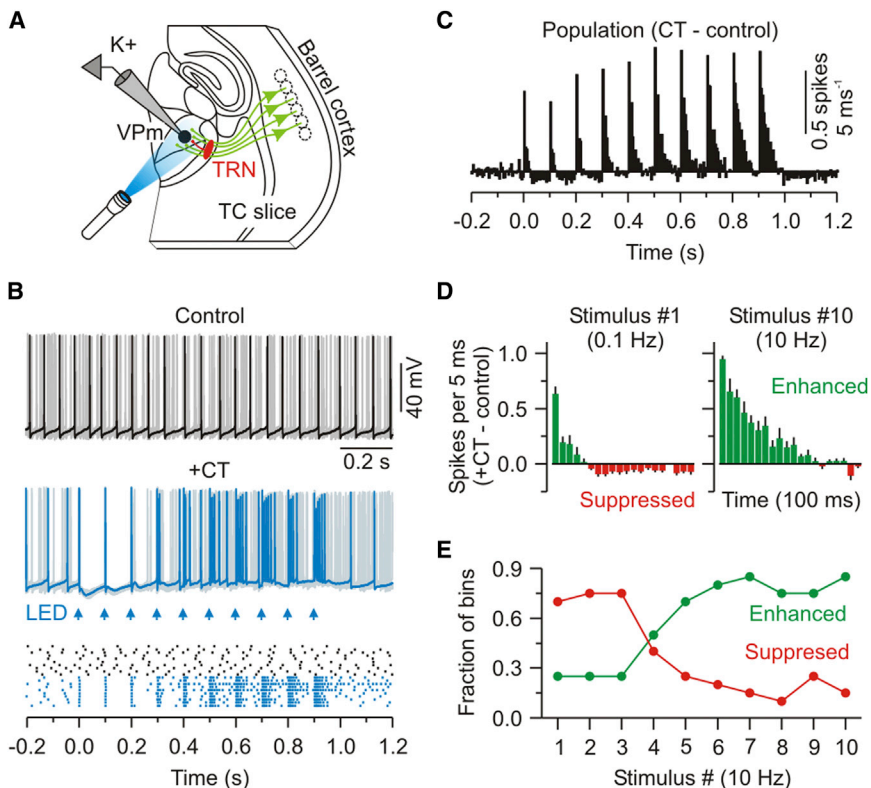
Figure 2. Trains of Optical CT Stimuli Initially Suppress and Later Enhance VPm Excitability

(A) Schematic of the recording configuration.

(B) The same conditions as in Figure 1D except for repetitive CT activation (10 Hz, arrows). Notice the transition of the CT effect from suppression to enhancement of spiking across the train.

(C) Population PSTH (5-ms bins) plotting the difference in spike rates for CT versus control trials (n = 12 cells from 6 mice).

(D) Population PSTH showing the initial 100 ms of response after the first and tenth CT stimuli. Data are represented as mean ± SEM.

(E) Fraction of bins in which the spike rates were suppressed (red) or enhanced (green) by CT stimulation versus stimulus number (bin counts were taken from the population plot shown in (C).

higher-frequency CT activity within the plausible in vivo range, we performed optical stimulation with 10-Hz trains (every 10 s) and measured the effects on ongoing VPm spiking as in the previous excitability tests (Figures 2A–2C). The first stimuli of the trains triggered brief initial windows of increased excitability followed by more protracted suppression, as under the low-frequency condition. Following subsequent stimuli in a train, however, enhancement intensified dramatically, whereas suppression dissipated, so that maximal spiking occurred toward the ends of the trains (Figures 2D and 2E). Together, these data indicate that CT effects on VPm excitability are regulated dynamically, mainly generating suppression at low frequencies or following long pauses but switching to net enhancement during even brief periods of high-frequency CT activity.

Synaptic Conductances Underlying CT Modulation of Thalamic Excitability

We used voltage-clamp recording to analyze the CT-activated synaptic conductances in VPm cells. Optical CT stimuli were again delivered in 10-Hz trains once every 10 s. These CT trains evoked dynamically evolving postsynaptic conductances in VPm cells that were highly consistent with the patterns of modulation described above. The first CT stimulus in each train caused a brief monosynaptic excitatory postsynaptic conductance (EPSG) that was dwarfed within a few milliseconds by a much larger and longer-lasting disynaptic inhibitory postsynaptic conductance (IPSG, mediated by CT activation of TRN cells) (Figures 3A–3C). The latency difference between the EPSG and IPSG onsets was 2.3 ± 0.1 ms (n = 8) (Figures 3B

and 3C). On average, the IPSG exceeded the EPSG within 2.8 ± 0.1 ms and remained higher until the next stimulus. Therefore, the net synaptic input to VPm neurons evoked by low-frequency CT activity is overwhelmingly inhibitory. As stimuli continued at 10 Hz, there was a radical shift in CT-evoked conductances. The EPSGs underwent robust short-term facilitation, whereas the IPSGs were strongly depressed ($EPSG_{10}/EPSG_1$, 3.60 ± 0.29; $IPSG_{10}/IPSG_1$, 0.31 ± 0.01; Figures 3B–3D). This resulted in progressively increasing excitatory/inhibitory ratios in VPm cells throughout a train.

To rule out the possibility that optogenetic methods of stimulation caused abnormal short-term dynamics, we compared EPSCs evoked by optical and electrical 10-Hz CT stimuli in the same VPm cells. The two modes of activation produced similar short-term dynamics with no significant differences (electrical versus optical, p > 0.10, paired t test; Figure S3). Moreover, short-term facilitation of CT-EPSPs was stronger in VPm than in TRN cells, consistent with previous studies (Figure S4; Cruikshank et al., 2010; Jurgens et al., 2012). Therefore, under the present experimental conditions, ChR2-expressing CT axons appear to produce normal response dynamics when stimulated optically at 10 Hz.

To clarify whether the combined synaptic input could account for the modulation of excitability seen previously in current-clamp recordings (Figures 2B–2E), we measured the pattern of mixed synaptic currents generated in VPm cells when their membrane potentials were held near the spike threshold (~-35 mV) (Normand et al., 2013). At this potential, responses were initially dominated by outward/inhibitory current, but, by the end of the train, inhibition had depressed, excitation had facilitated, and the net current became inward/excitatory (n = 7 cells from 3 mice; Figures 3E and 3F), consistent with the modulation of VPm excitability. Curiously, the mixed current had greater net excitation than that predicted by linear extrapolation from the pure EPSGs and IPSGs measured at the inhibitory and excitatory
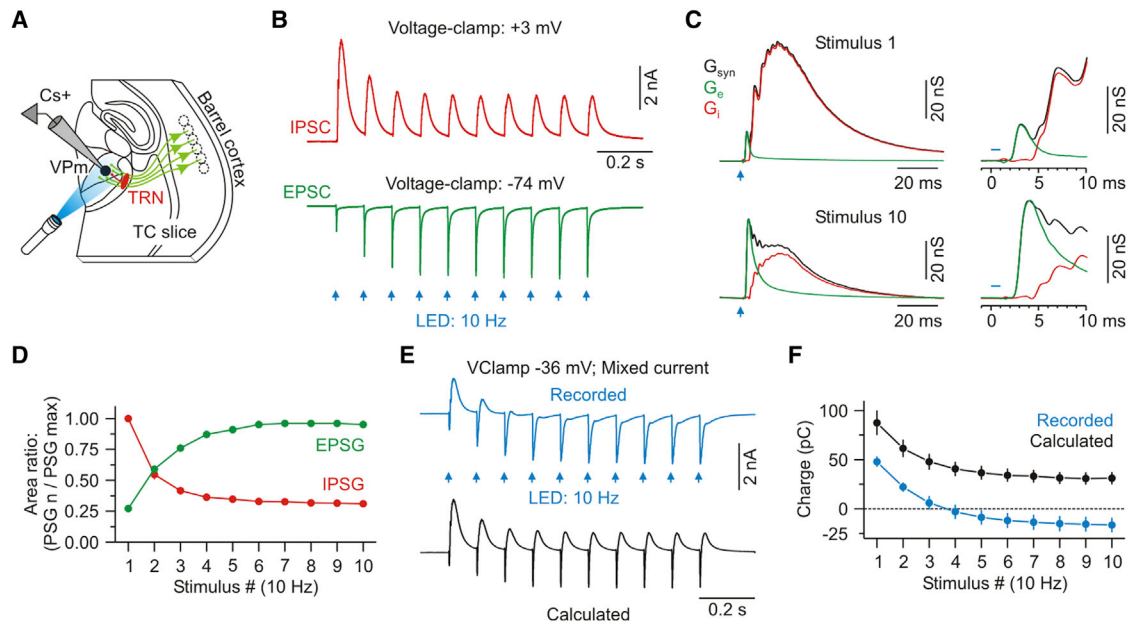
Figure 3. Synaptic Excitation Increases as Inhibition Decreases in VPm Cells during Repetitive CT Activation

(A) Schematic of the recording configuration.

(B) IPSCs and EPSCs evoked in a VPm cell by 10-Hz optical activation of CT axons (average of 20 trials). Shown are EPSCs and IPSCs recorded at reversal potentials for inhibition (−74 mV) and excitation (+3 mV), respectively (Cs+ internal solution).

(C) Average excitatory (G_e, green) and inhibitory (G_i, red) components of the total synaptic conductance (G_{syn}, black) evoked by the first and tenth CT stimuli (the same cell as in B). The insets show the initial 10 ms of the responses.

(D) Population data showing the short-term dynamics of CT-EPSGs and disynaptic IPSGs evoked in VPm cells (n = 8 cells).

(E) Top: mixed synaptic current recorded in a VPm cell voltage-clamped near the spike threshold (−36 mV). Bottom: calculated current, predicted for that same holding potential (−36 mV), based on linear extrapolation from the pure EPSGs and IPSGs plotted in (B).

(F) Population data showing the net charge resulting from the recorded and calculated/predicted current for each stimulus number (100 ms post-stimulus, n = 7 cells). Data are represented as mean ± SEM.

See also Figures S3 and S4.

synaptic reversal potentials (Figures 3E and 3F; calculated). The apparent nonlinearity, manifested by the strong inward currents recorded near the spike threshold, could be caused by the activation of *N*-methyl-D-aspartate receptors (NMDARs). In fact, NMDARs are present at the CT-VPm synapse (Deschênes and Hu, 1990; Kao and Coulter, 1997; Miyata, 2007; Pedroarena and Llinás, 2001; Scharfman et al., 1990), and there is evidence that NMDA spikes can be elicited in distal dendrites of thalamic relay cells, where the majority of CT terminals are located (Augustinaite et al., 2014; Liu et al., 1995).

To fully characterize the CT-evoked excitatory currents in VPm cells, EPSCs were recorded over a range of potentials while blocking GABAergic transmission. This revealed that the integrated EPSC-voltage relationship had a region of negative slope conductance between −70 and −30 mV, reminiscent of the current carried by NMDARs (n = 6 cells from 5 mice; Figures 4A–4C; Mayer et al., 1984; Nowak et al., 1984). Subsequent isolation of the NMDAR and AMPA receptor (AMPAR) components with the selective antagonists DNQX (n = 2) and APV (n = 4) revealed that NMDARs carry the majority of CT-evoked excitatory current in VPm cells at voltages near and above the spike threshold (~70% of the total charge), with AMPARs dominating only at more hyperpolarized potentials (Figures 4A–4C). Like the control EPSCs, the isolated AMPAR- and NMDAR-mediated currents

underwent strong short-term facilitation (e.g., Figure 4D). In the presence of both DNQX and APV, the CT-evoked excitatory current was reduced by at least 95% (n = 6 of 6 cells; Figure 4B).

The voltage-clamp data showed that the overall pattern of CT synaptic input to VPm cells correlated well with the modulation of their excitability and suggested that NMDA receptors at the CT-VPm synapses could be particularly important. To more directly test the roles of the individual CT-evoked synaptic conductances (including their short-term plasticity) in VPm modulation, we turned to dynamic clamp (Prinz et al., 2004). The AMPAR-, NMDAR-, and GABA$_A$R-mediated conductances were manipulated independently in the recorded VPm cells, and effects on excitability were measured (Figure 4E).

First we tested the effects of applying a standard set of simulated CT conductances consisting of a 10-Hz train of excitatory (AMPA and NMDA) and inhibitory (GABA) conductances derived directly from the voltage-clamp recordings (Figures 3 and 4A–4D). Modulation of VPm spiking by this standard set was very similar to the modulation caused by optical CT stimulation (n = 14 cells from 6 mice; Figures 2 and 4F), providing support for the general approach. Subsequent removal of the NMDA conductance selectively and strongly attenuated the late enhancement of VPm spiking while leaving the early modulation unaffected (n = 11 cells; Figure 4G). Nearly identical results were
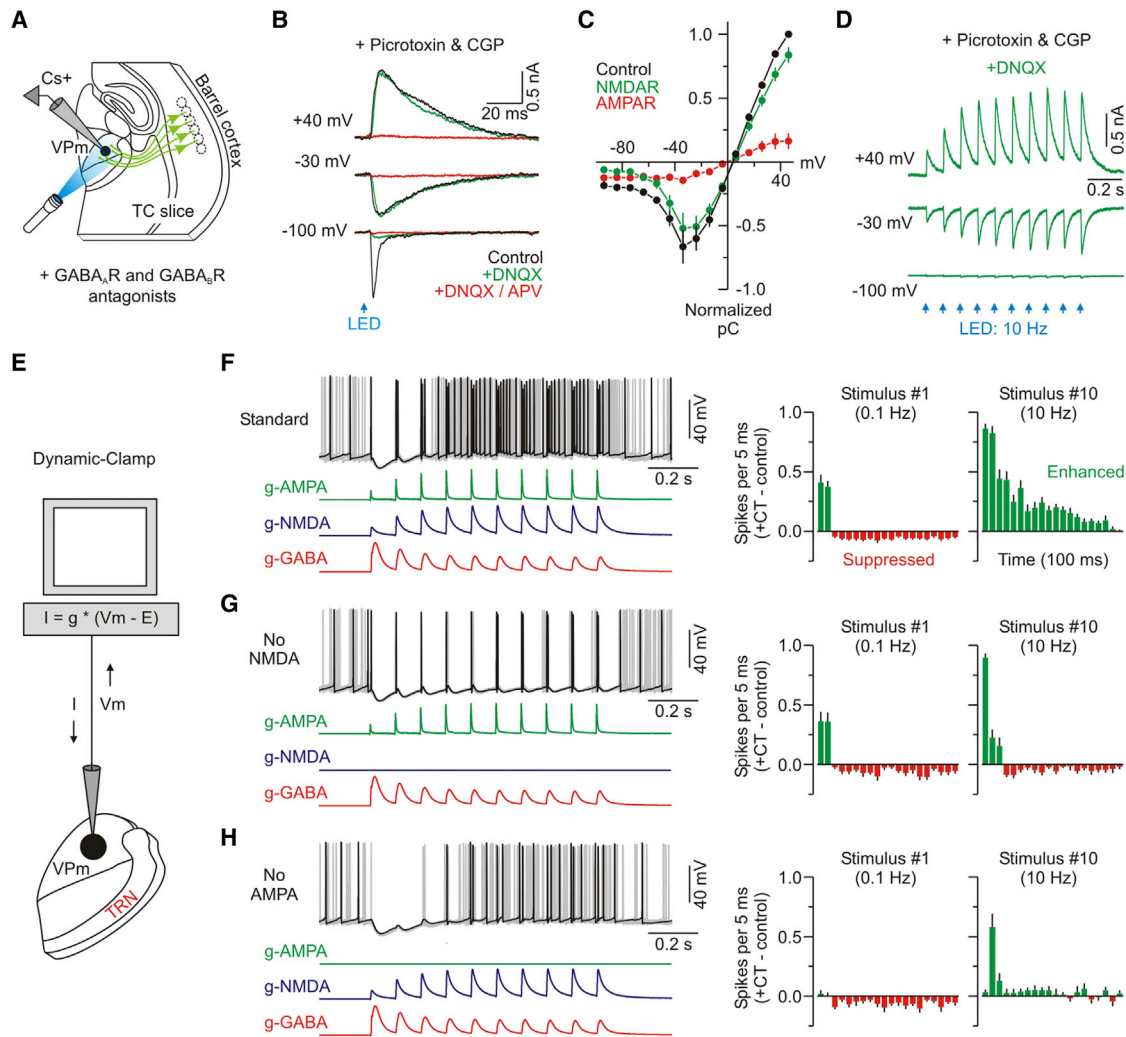
Figure 4. The Role of Fast Glutamate Receptors in CT Modulation of VPm Excitability

(A) Schematic of the recording configuration. Inhibitory transmission was blocked by applying GABA$_A$ and GABA$_B$ receptor antagonists (picrotoxin, 50 μM; CGP-55845, 2 μM).

(B) CT-evoked EPSCs from a VPm cell under control, DNQX, and DNQX + APV conditions at the indicated membrane potentials (DNQX, 20 μM; APV, 50 μM).

(C) Population plot showing the integrated current-voltage relationship for the CT-evoked EPSC (control) as well as the isolated NMDAR and AMPAR components of the response (n = 6 cells from 5 mice). NMDAR-mediated responses were isolated by applying DNQX (n = 2) and measuring the response that remained or by applying APV (n = 4) and subtracting the response that remained from the control response. AMPAR-mediated responses were isolated similarly (n = 4 APV cells, n = 2 DNQX cells).

(D) Isolated NMDAR-mediated synaptic current in response to repetitive 10-Hz optical activation of CT axons (DNQX was present in the bath).

(E) Schematic of the recording configuration. Dynamic-clamp recording was used to compute a real-time current (I) output based on the recorded membrane potential (Vm) and three modeled CT-evoked conductances (g-AMPA, g-NMDA, and g-GABA). Standard conductance waveforms were based on previously recorded data evoked by optical CT stimulation (Figures 3B and 4B–4D).

(F) The same type of excitability experiment as described in Figure 2. Left: overlay of ten sweeps from a VPm cell with the three standard CT conductances applied. Trials with control spiking activity (i.e., no CT conductances) are not shown but were interleaved during testing. Right: population PSTHs (5-ms bins) plotting difference in spike rates for the trials with CT conductances versus control trials (n = 14 cells from 6 mice). The two plots show the initial 100 ms of response after the first and tenth CT stimuli.

(G) A similar excitability experiment, but the g-NMDA was removed (n = 11 cells from 6 mice). See also Figures S5 and S6.

(H) A similar excitability experiment, but the g-AMPA was removed (n = 10 cells from 6 mice).

Data are represented as mean ± SEM.

obtained when APV was used to block NMDARs during optical CT stimulation (Figure S5), confirming that large NMDAR currents enhance VPm excitability. Interestingly, selective removal of the AMPA conductance, which accounted for only ∼30% of

the total current near the spike threshold, strongly attenuated both the early and late modulation of VPm spiking (n = 10 cells; Figure 4H). These results indicate that, despite differences in overall charge, activation of both NMDARs and AMPARs is

necessary for the full switching of VPm excitability by higher-frequency CT inputs. The two conductances apparently act in concert, and AMPARs may provide the "priming" current required to depolarize VPm cells into the NMDAR activation range (MacDermott and Dale, 1987).

Is it possible that the unique channel-gating properties of NMDARs are critical for the CT-evoked late enhancement of VPm excitability? Besides total amplitude, there were two main differences between the CT-evoked NMDAR and AMPAR conductances. First, NMDARs had a nonlinear voltage dependence, conducting much more strongly at depolarized than hyperpolarized potentials (Figures 4B and 4C). This could provide a positive feedback mechanism to enhance VPm spiking during high-frequency CT input. Second, NMDAR currents were kinetically slow and long-lasting (Figure 4F), potentially providing inward current to overcome late GABA conductances. We used dynamic clamp to test each of these features in turn. Surprisingly, when the voltage dependence of the NMDAR conductance was eliminated (making it ohmic), the resulting modulation of VPm spiking was nearly identical to the NMDA standard (Figure S6C). Furthermore, speeding up the NMDA kinetics (to match AMPA kinetics) had only modest effects (Figure S6D). Therefore, although NMDARs (and AMPARs) are clearly important for the postsynaptic transformation of CT input, these data suggest that the unique biophysical properties of NMDARs are not essential to the switching of VPm excitability under the circumstances of our studies.

Role of Short-Term Dynamics in Modulation of VPm Excitability

The short-term dynamics of the CT synaptic conductances (i.e., facilitation of excitation and depression of inhibition) appeared to parallel the CT modulation of VPm excitability, as described above. To test the causal relationship between these synaptic dynamics and the changes in excitability, we simply held either the simulated EPSGs or IPSGs constant within the trains and measured the effects on VPm spiking (Figure 5A). Replacing the facilitating CT-evoked excitatory conductances with stable EPSGs essentially eliminated the late enhancement in VPm excitability (n = 6 cells from 4 mice; Figure 5C). Replacing the depressing disynaptic inhibitory conductance (g-GABA) with flat dynamics produced a similar, although less extreme, effect (n = 7 cells; Figure 5D).

Together, the results indicate that the dynamic pattern of synaptic inputs to VPm cells can account almost completely for the CT-triggered modulation of their excitability. These synaptic inputs switch their net sign in an activity-dependent way. They are predominantly inhibitory during low-frequency CT activity (≤0.1 Hz) and excitatory at higher frequencies (~10 Hz). This shifting depends on the combination of two dynamic phenomena: facilitation of monosynaptic CT-evoked EPSCs and reduction of CT-triggered disynaptic IPSCs.

Mechanisms of Decreasing Inhibition in VPm during Repetitive CT Activation

Short-term facilitation is an established property of L6 CT excitatory synapses and has been fairly well characterized (Beierlein and Connors, 2002; Deschênes and Hu, 1990; Ferster and Lindström, 1985; Landisman and Connors, 2007; Sun and Beierlein,

2011; Turner and Salt, 1998; von Krosigk et al., 1999). But why does sustained activity in the CT circuit lead to decreased inhibition of the VPm? To determine this, we examined the transformation of CT signaling through the cells that mediate the inhibition: TRN cells.

In response to optical CT stimulation at 10 Hz, TRN cells generated robust EPSCs that exhibited clear short-term facilitation, consistent with previous reports (Figures 6A–6C; Figure S4; Jurgens et al., 2012). In contrast, there was essentially no detectable disynaptic inhibition in TRN cells (Figures 6B and 6C; Cruikshank et al., 2010; Olsen et al., 2012). We next tested how TRN cells transform this facilitating CT input into spike discharge using cell-attached recordings (which minimize cellular disturbances). The number of spikes evoked by sequential CT stimuli decreased significantly over the course of the trains (stimulus 1, 9.3 ± 0.7 spikes; stimulus 10, 5.8 ± 0.6 spikes; n = 6 from 2 mice; p < 0.01; paired t test; Figures 6D and 6E). This unexpected transformation appears to depend on the intrinsic burst properties of TRN cells and not on synaptic mechanisms because the excitatory synaptic input facilitated and did not depress, there was no apparent contribution by synaptic inhibition, and TRN cells responded to CT stimulus trains with increasing spike output when held at depolarized potentials (Figures S7A and 7B). The reduced TRN output is consistent with previous studies, which show that thalamic cell bursts are incapable of following at high frequency because of the intrinsic properties of the low-threshold calcium current (I_T) that underlies the bursts (Crunelli et al., 1989; Jahnsen and Llinás, 1984; Kao and Coulter, 1997; McCormick and Feeser, 1990; Pedroarena and Llinás, 2001). At high burst frequencies, I_T does not have sufficient time to fully recover from inactivation. We conclude that, from rest, TRN cells transform facilitating CT-EPSCs into decreasing spike output, and this is very likely because of the properties of I_T in these cells (Crandall et al., 2010; Huguenard and Prince, 1992). It seems unlikely, however, that the ~40% decrease in spike output would fully account for the ~70% reduction in synaptic inhibition recorded in VPm cells (Figure 3D).

Do short-term dynamics of the GABAergic TRN-VPm synapses also contribute to the reduced inhibition (Zucker and Regehr, 2002)? To test the properties of these synapses, we electrically stimulated TRN axons and recorded the resulting IPSCs in VPm cells. Inhibitory responses were isolated by blocking glutamatergic transmission and removing the TRN from the slice, which prevented intra-TRN processes from influencing responses (Figure 6F; Huntsman et al., 1999; Landisman et al., 2002). During simple train stimulation, the inhibitory synapses underwent remarkably strong short-term depression over a wide range of frequencies (Figure 6G). To assess how IPSCs change during the more complex TRN activity evoked by optical CT stimulation, we used a TRN-burst electrical stimulation protocol that mimicked the average TRN bursting pattern evoked by optical CT train stimuli. TRN burst electrical stimulation resulted in robust short-term depression. More importantly, the precise IPSC dynamics were nearly identical to those recorded during optical CT stimulation (Figures 6H and 6I). To estimate the degree to which TRN intrinsic properties (including decrementing spike counts per burst) contribute to the IPSC dynamics, we used a control burst electrical stimulation in which all bursts in
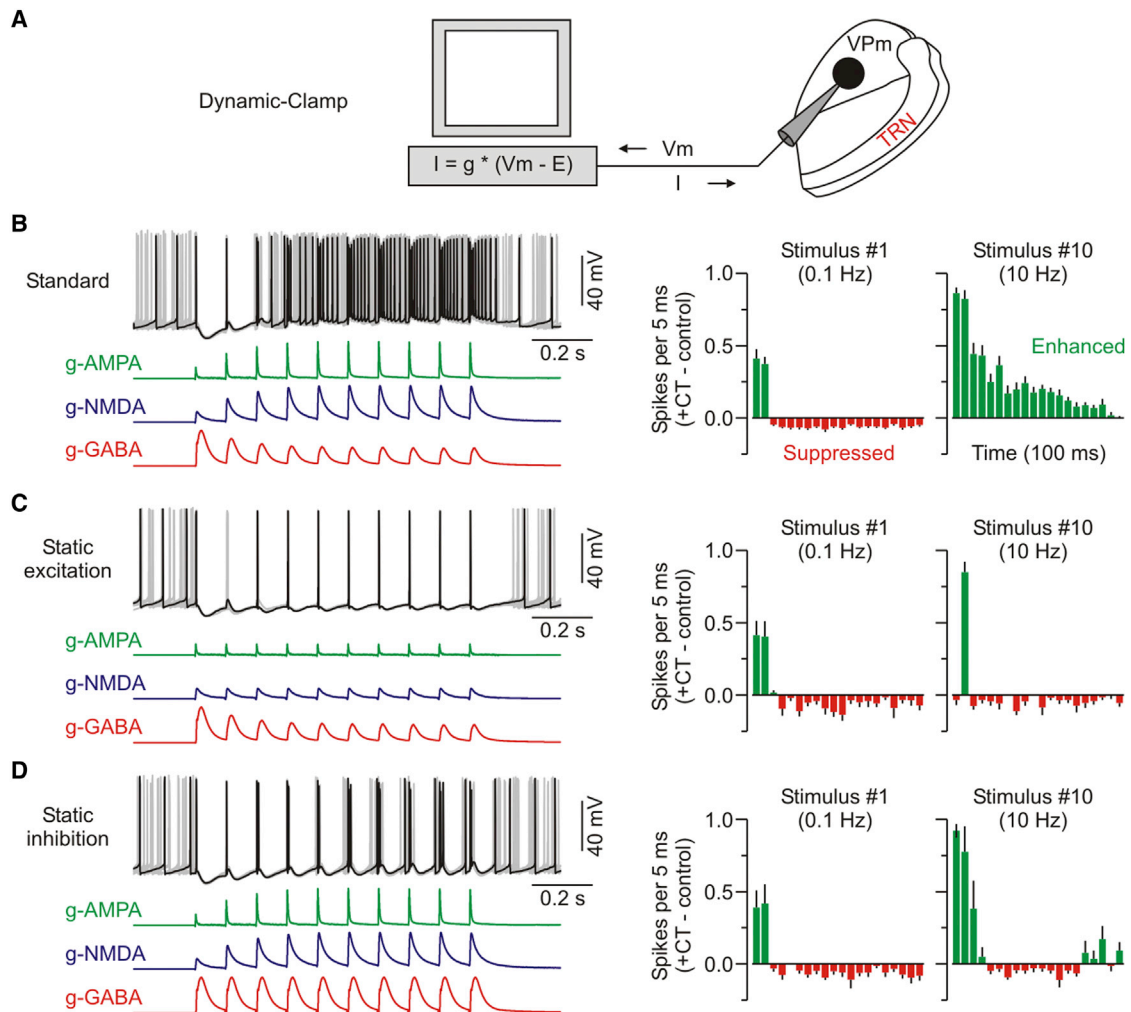
Figure 5. Synaptic Dynamics Can Account for Frequency-Dependent Switching in CT-Triggered Modulation of VPm Excitability

(A) The same recording configuration as described in Figure 4E.

(B) A different example of a cell but the same excitability experiment as described in Figure 4F. Left: overlay of ten sweeps in which dynamic-clamp recording was used to model the three standard CT-evoked conductances. Right: population PSTHs (5-ms bins) plotting the difference in spike rates (i.e., trials with CT conductances versus control trials) for the first and tenth CT stimuli (n = 14 cells from 6 mice).

(C) A similar excitability experiment as for the cell shown in (B), but short-term facilitation of the excitatory conductances (g-AMPA and g-NMDA) was removed by statically repeating the first conductances across the train (n = 6 cells from 4 mice).

(D) A similar excitability experiment as for the cell shown in (B), but short-term depression of the inhibitory conductance (g-GABA) was removed, again by repeating the first conductance across the train (n = 7 cells from 4 mice).

Data are represented as mean ± SEM.

the train were identical (9 pulses, 350 Hz). Again, IPSCs recorded in VPm cells depressed significantly, nearly matching those recorded during optical CT stimulation (Figure 6I). Therefore, the decreasing IPSCs recorded during optical CT train stimuli are primarily explained by the robust short-term synaptic depression of the TRN-VPm synapse, with only a minimal contribution from the intrinsically mediated reductions in TRN spiking.

Effects of Cortical Gamma-Band Activity on the Thalamus

We next asked whether the CT-mediated shifts in excitability of VPm cells would also emerge during patterns of cortical activity

that have been reported in alert animals, such as gamma-band activity (Briggs and Usrey, 2009a; Steriade et al., 1996). Cortical gamma activity is thought to enhance sensory processing by sharpening temporal spike precision within groups of cells projecting to common targets (Cardin et al., 2009; Fries, 2009). To generate such activity in the CT pathway and avoid the type of highly synchronized activity that seems to occur during pulsatile stimulation of presynaptic terminals, we locally activated ChR2-expressing CT cells within L6 using ramps of light (1-s duration, 250-μm spot diameter). Similar ramp stimuli have been shown to elicit sustained gamma frequency oscillations in cortical circuits (Adesnik and Scanziani, 2010). To determine how light

ramps affect L6, we used whole-cell current-clamp recordings to monitor spiking in ChR2-expressing CT cells and local field potentials (LFPs) to monitor population activity (Figure 7A). Ramps of light were very effective in triggering sustained spiking in CT cells (18.2 ± 3.3 spikes per 1-s ramp stimulus; range, 5.2–39.2 spikes; n = 9 of 6 mice; Figure 7B) and oscillatory LFP activity in the high gamma range (75.5 ± 1.1 Hz; Figures 7B and 7C). Spikes in L6 CT cells were phase-locked with the LFP oscillations (Figure 7D). When CT cells were voltage-clamped to isolate the underlying synaptic currents, fast oscillatory IPSCs were revealed (Figures 7E and 7F), and they were also phase-locked with the LFPs (Figure 7G). Therefore, ramps of light effectively drive sustained spiking in CT neurons and gamma oscillations in L6. Moreover, unlike pulsatile stimulation of presynaptic terminals, which appears to produce highly synchronized CT output that passively follows the temporal details of the stimuli, the CT output pattern produced by light ramp stimulation is determined largely by active synaptic interactions within the cortical network and appears to generate less synchronized output from CT cells. Spike failures typically occur on more than half of the gamma cycles for any given CT cell.

We tested the effect of cortical gamma activity on the thalamus by recording from VPm cells in slices that conserved connectivity between the barrel cortex and VPm and stimulating the aligned cortical barrels with light ramps (Figure 8A). This resulted in large barrages of EPSPs and IPSCs in VPm cells, which led to a significant increase in their membrane potential variance (dark, 0.2 ± 0.1 mV; light, 5.3 ± 0.9 mV; n = 13 cells from 6 mice; p < 0.001; Wilcoxon paired signed-rank test) and net depolarization by the end of the 1-s ramp (from rest ∼−74 mV, 6.4 ± 1.2 mV; n = 13 cells from 6 mice; Figure 8B). Of the 13 VPm cells recorded, 9 (69%) were driven to the spike threshold. When a VPm cell and an aligned L6 CT cell were recorded simultaneously, spike-triggered averages revealed that CT spikes occurred 7.4 ms before the peaks of the VPm-EPSPs (Figure 8C). When VPm cells were voltage-clamped to isolate CT-EPSCs, fast oscillatory currents were revealed (peak frequency, 75.2 ± 2.8 Hz; Figures 8D and 8E). Moreover, these EPSCs recorded in VPm correlated strongly with the LFPs recorded in L6 (Figure 8F). In a subset of cells (n = 3), CT gamma activity also initiated a brief but clear oscillation of ∼10 Hz, presumably generated by the intrathalamic TRN-VPm circuit (Huguenard and McCormick, 2007; Leresche et al., 2012; Steriade et al., 1993; Figures 8B, 8G, and 8H; Figure S8).

Bouts of gamma activity in cortical L6 progressively shifted the excitability of VPm cells (Figure 8B). To assess this, tonic spiking (∼11 Hz) was induced in VPm cells with injected current, and spiking patterns were compared for trials with and without ramps of light over L6. In the majority of cases (7 of 11 cells), ramps of light suppressed VPm spiking during the first few hundred milliseconds after onset but had an enhancing effect by the end of the ramp (Figure 8G). Therefore, the modulation by self-sustained network activity in L6 was similar to the effects of 10-Hz optical CT stimuli. Modulation by the ramp stimulation never occurred in the reverse direction (i.e., early enhancement, later suppression), although, in 4 of 11 cells, it was predominantly unidirectional (suppression in two cells and enhancement in two cells). Voltage-clamping VPm cells at a depolarized potential (−54 mV) to record the mixed synaptic currents underlying these effects revealed a shift in the sign of the net currents from early IPSCs to late EPSCs (Figures 8H and 8I). Once again, the effects of sustained L6 activity on the VPm were similar to those induced by 10-Hz optical CT stimulation.

DISCUSSION

The cortex is a major source of excitatory input to the thalamus, but a basic understanding of how cortical input regulates thalamic processing has been elusive. Using selective optogenetic activation of L6 CT cells in the mouse somatosensory system, we found that cortical influences on thalamic excitability are dynamic, switching from suppression to enhancement in an activity-dependent fashion. A targeted analysis of the specific cells and synapses involved in CT processing revealed that a simple yet robust set of circuit mechanisms underlies these effects.

During low-frequency CT activity, or after long pauses, there is an initial transient excitation of VPm cells that briefly increases spike probability. However, excitation is quickly followed by a strong and long-lasting inhibition that suppresses spiking. This occurs because the relatively weak monosynaptic excitatory CT input onto thalamic relay cells is dwarfed by robust disynaptic inhibition from TRN neurons. In contrast, during high-frequency CT activity the overall excitation and spiking probability of the thalamic relay cells increases. This happens for two reasons. First, monosynaptic excitatory CT input facilitates with activity. This facilitating excitation is largely carried by NMDAR-mediated currents, which dominate the monosynaptic response. Second, disynaptic inhibitory input from TRN decreases, mainly because of short-term depression of the GABAergic TRN synapses. Although TRN spike rates are also reduced during high-frequency CT activity, the functional consequences of this reduction are clearly outweighed by synaptic depression of the GABAergic synapse itself. Together, these results demonstrate how the cortex can serve as a dynamic activity-dependent gatekeeper of its own sensory input.

CT cells are known to have a range of conduction velocities (Beierlein and Connors, 2002; Briggs and Usrey, 2009b; Swadlow, 1989; Swadlow and Weyand, 1987). Therefore, under conditions in which CT spikes are initiated intracortically (rather than locally within the thalamus, as done in the majority of experiments here), it is likely that the initial transient excitation could become blunted because of a reduced synchrony of input from CT axons with different conduction velocities. This might shift the overall balance even further toward inhibition during low-frequency CT activation, causing an even starker functional contrast between low- and high-frequency states.

Previous in vivo studies examining the role of L6 CT projections from somatosensory cortex have reported varying effects (Diamond et al., 1992; Ghosh et al., 1994; Yuan et al., 1986). Much of this variability has been attributed to the functional topography of the CT pathway (Deschênes et al., 1998). For example, in the whisker-barrel system, activity in a single cortical column enhanced the activity of functionally aligned VPm cells (that is, cells tuned to the same deflection angle or principal whisker) and suppressed the activity of non-aligned VPm cells
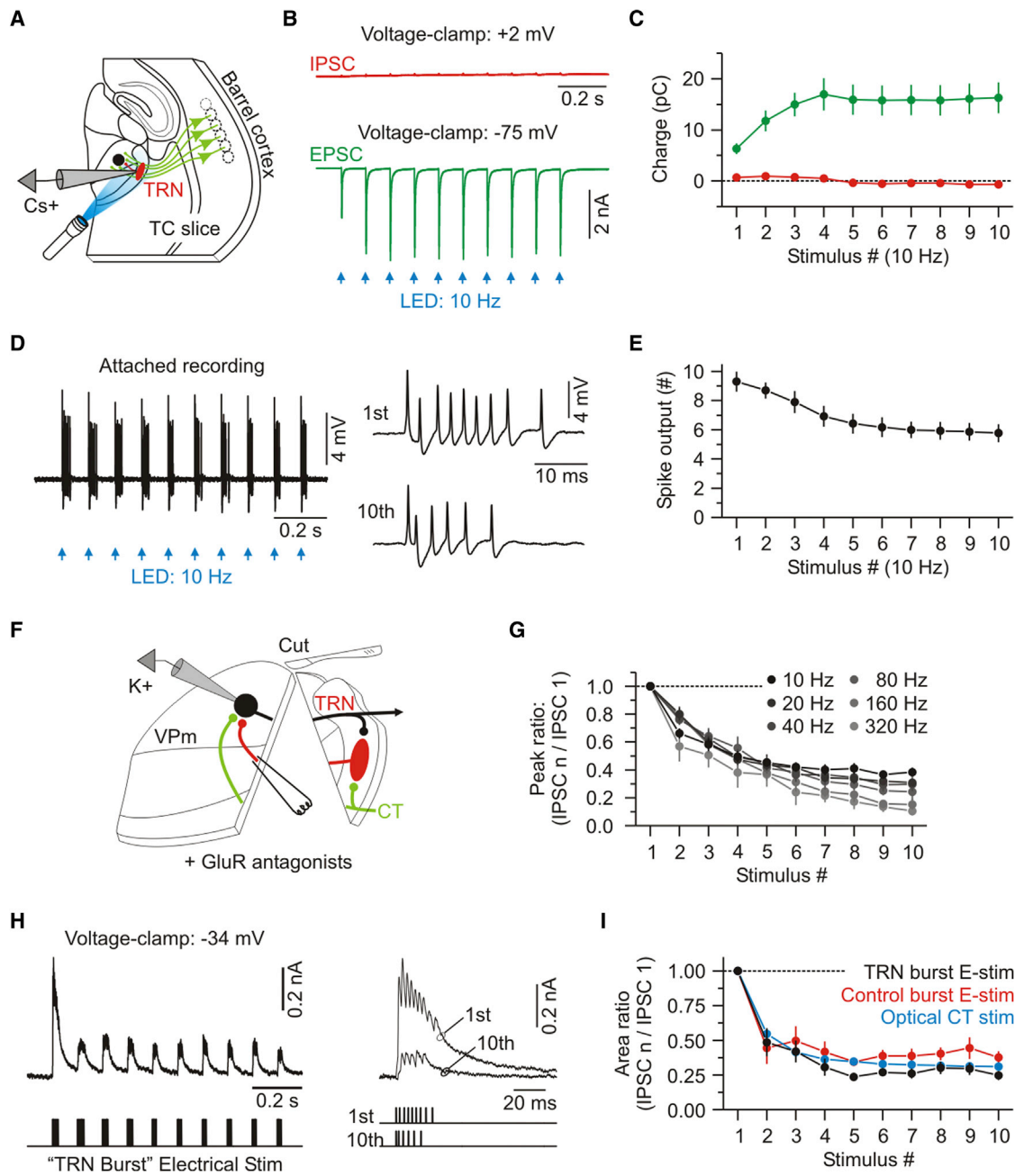
Figure 6. Mechanisms of Dynamic Reduction of CT-Mediated Inhibition in VPm Cells

(A) Schematic of the recording configuration.

(B) IPSCs and EPSCs from a TRN cell in response to repetitive optical activation of CT axons (average of 20 trials, Cs^+ internal solution).

(C) Population plot showing the average synaptic charges for each stimulus (n = 5 cells from 2 mice).

(D) TRN spike responses (cell-attached) to repetitive optical CT stimulation. For display, the trace was high pass-filtered (100 Hz). Right: responses to the first and tenth stimuli.

(E) Population plot showing the number of action potentials discharged by TRN cells versus stimulus number (n = 6 cells from 2 mice). See also Figure S7.

(F) Electrical stimulation of cut TRN axons and whole-cell recordings from VPm cells and schematic of the recording configuration. Glutamate receptors were blocked (20 μM DNQX, 50 μM APV). IPSCs were measured at −34 or −39 mV.

(G) Population IPSC dynamics from VPm cells (n = 13 cells from 4 mice) in response to simple electrical train stimulation of TRN axons across a range of fixed frequencies.
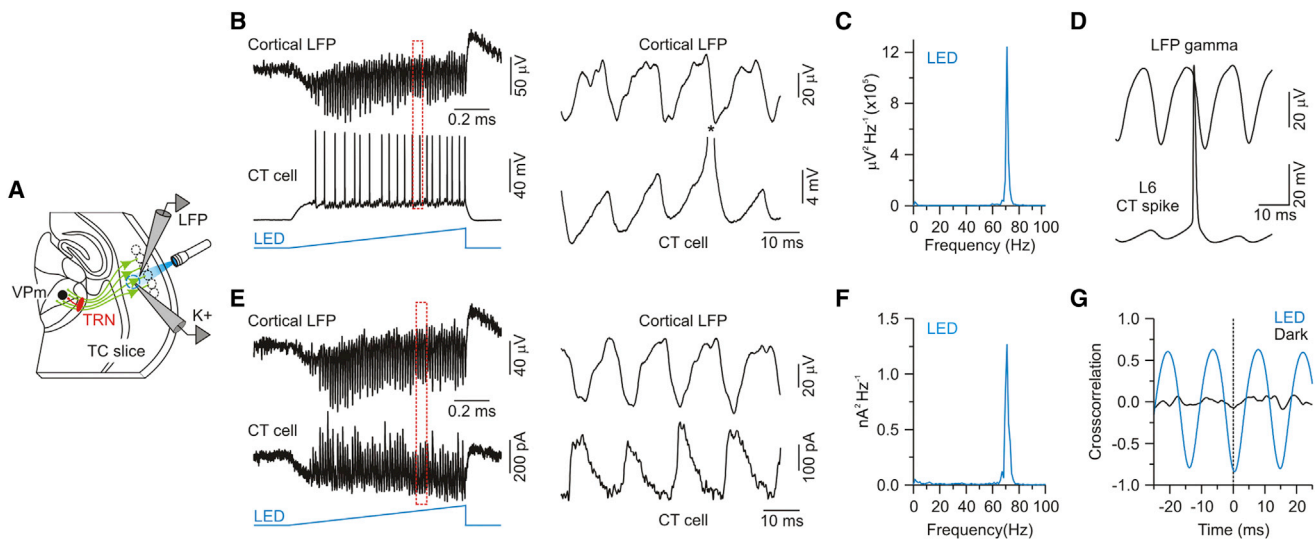
(legend continued on next page)

Figure 7. Sustained Optogenetic Activation of CT Cells in L6 Generates Local Network Gamma Rhythms

(A) Schematic of the recording configuration.

(B) Left: simultaneous LFP and intracellular recording of a ChR2-expressing CT cell in L6 during light ramp stimulation (1 s). The LFP electrode was located in L5b, at the level of CT cell apical dendrites. Right: expanded traces of the period, indicated by the dashed red rectangle. The asterisk indicates the truncated spike.

(C) Average LFP power spectrum for the same recording session as shown in (B) (7 sweeps). For display, data were high pass-filtered (2 Hz).

(D) Spike-triggered LFP averages for the LFP cell pair in (B) (114 spikes). Similar spike-LFP phase-locking occurred in 6 of 6 cells (from three mice).

(E) Left: simultaneous LFP and intracellular voltage-clamp recording (from −54 mV) of a ChR2-expressing CT cell during light ramp stimulation (1 s). Right: expanded traces of the period, indicated by the dashed red rectangle.

(F) Average IPSC power spectrum for the LED condition for the same recording session as shown in (E) (7 sweeps). For display, data were high pass-filtered (2 Hz).

(G) Cross-correlation of IPSCs and LFP during light ramp stimulation for the same LFP cell pair as shown in (E). IPSCs recorded in L6 CT cells were strongly phase-locked with the locally recorded LFP (peak negative correlation, −0.67 ± 0.05; n = 5 cells from 3 mice).

Data are represented as mean ± SEM.

(Li and Ebner, 2007; Temereanca and Simons, 2004). However, our results imply a subtler role of CT activity on the thalamus. They suggest that, in addition to spatial precision, the influence of CT activity also has temporal precision that can bidirectionally alter the net sign of the aligned CT influence (i.e., excitation versus inhibition), depending on the time and on the frequency of CT firing.

How could the cortex impact its own sensory input through L6 CT cells? Lower CT firing rates evoke small membrane depolarizations, followed by larger hyperpolarizations because of longer-lasting IPSPs. This should mainly suppress the sensory-mediated thalamic drive of the cortex. In contrast, the EPSPs evoked by higher rates of CT firing should, in turn, enhance sustained sensory-driven spiking among associated thalamic cells by reducing the response adaptation to repetitive sensory stimulation (Mease et al., 2014; Sillito et al., 1994). This CT-mediated enhancement of thalamic throughput would improve the thalamic drive of cortical neurons (Alonso et al., 1996; Bruno and Sakmann, 2006; Cruikshank et al., 2007), potentially

including CT cells themselves (Cruikshank et al., 2010; Yang et al., 2014). However, it is worth noting that, in certain resting membrane states (Hirsch et al., 1983; Jahnsen and Llinás, 1984; Steriade et al., 1993), the strong CT-mediated inhibition evoked by lower rates of CT firing could also promote sensory-driven bursts in relay cells (Figures S2F–S2H), which strongly activate cortical circuits and may serve as a "wakeup call" for the cortex (Guido and Weyand, 1995; Swadlow and Gusev, 2001; Usrey et al., 2000).

We also found that brief periods of sustained activity in L6 can generate a local cortical gamma rhythm that, via CT cells, can quickly shift the cortical effect on thalamic throughput from suppression to enhancement. This is an intriguing observation given reports that cortical gamma oscillations can be evoked by sensory stimuli during states of focused attention or alertness (Bastos et al., 2014; Fries, 2009; Singer, 1993). Moreover, there is evidence that directed attention can modulate thalamic activity (McAlonan et al., 2008; O'Connor et al., 2002). Although the functions and mechanisms of gamma rhythms are debated, there is

(H) Left: IPSCs from a representative VPm cell in response to "TRN burst" electrical stimulation. This pattern of stimulation matched the average burst pattern recorded previously from TRN cells in response to optical CT activation (during attached recordings as in D and E, average of 20 sweeps). Right: overlay of the responses to the first and tenth stimulus. Electrical artifacts were removed.

(I) Mean IPSC dynamics of six cells (from two mice) stimulated electrically with the TRN burst pattern and a control burst pattern that consisted of nine synaptic pulses at 350 Hz repeated at 10 Hz. Also shown are IPSC data collected from the optical CT stimulation condition (blue, from Figure 3).
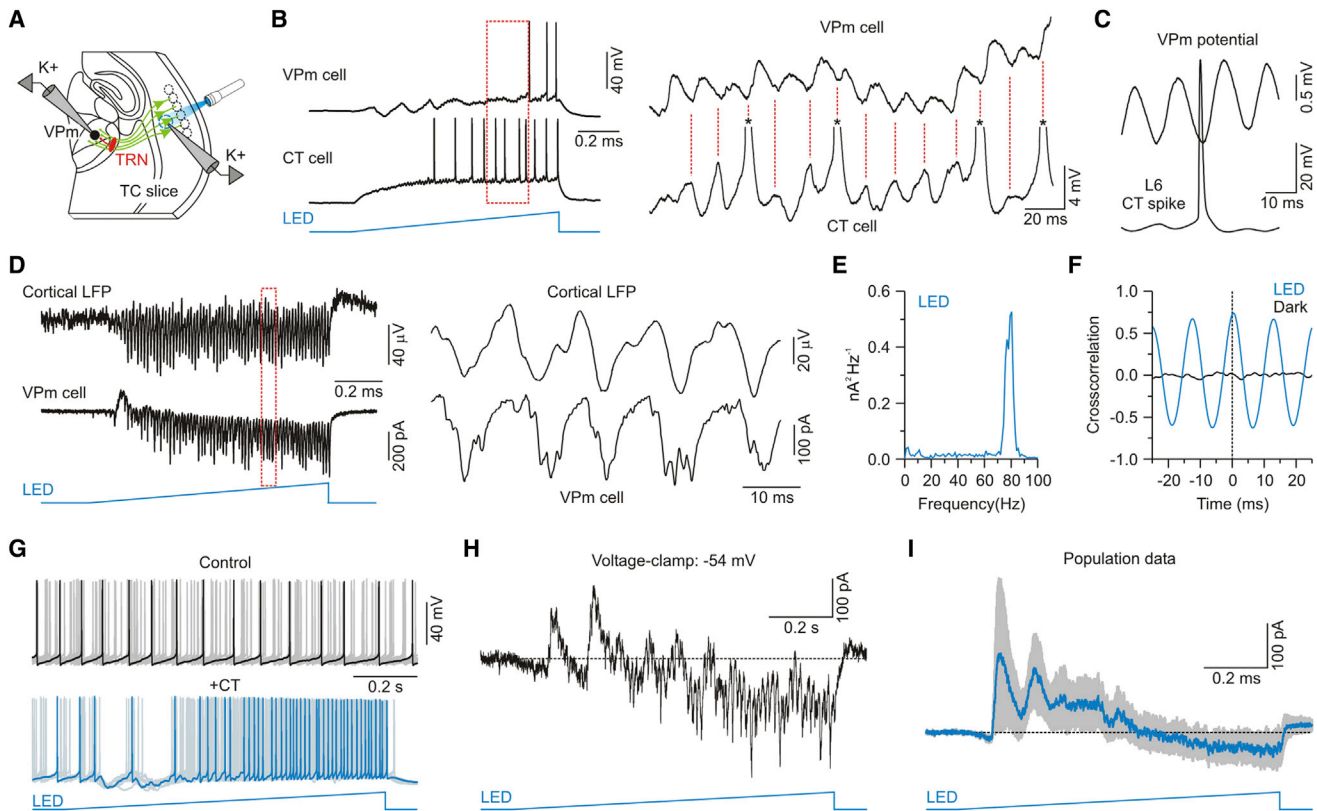
Data are represented as mean ± SEM.

Figure 8. Gamma-Band Activity in the CT L6 Network Initially Suppresses and Then Enhances VPm Excitability

(A) Schematic of the recording configuration.

(B) Left: simultaneous intracellular recording of a ChR2-expressing CT cell and ChR2-negative VPm cell during light ramp stimulation over L6. The pair was not monosynaptically connected. Right: expanded traces of the period, indicated by the dashed red rectangle. The asterisks indicate truncated spikes.

(C) Spike-triggered potential averages for the CT-VPm pair shown in (B) (47 spikes).

(D) Left: simultaneous LFP from the cortex and intracellular voltage-clamp recording (−89 mV) from a ChR2-negative VPm cell during light ramp stimulation over L6 (1 s). Right: expanded traces of the period, indicated by the dashed red rectangle.

(E) Average power spectrum of synaptic currents during LED stimulation for the VPm recording session shown in (D) (6 sweeps). For display, data were high pass-filtered (2 Hz).

(F) Cross-correlation of VPm EPSCs and cortical LFP during light ramp stimulation for the LFP cell pair shown in (D). EPSCs recorded in VPm cells were strongly correlated with the L6 LFP (peak correlation, 0.59 ± 0.12; n = 2 cells from 2 mice).

(G) Top: overlay of ten sweeps from a VPm cell during injection of depolarizing current. Bottom: the same cell with the same current injection during a 1-s light ramp over L6.

(H) Mixed synaptic currents (V_m, −54 mV) from the cell shown in (G).

(I) Average synaptic current (blue trace, SEM shown in gray) evoked by optical ramp stimulation for the seven cells tested in voltage-clamp recordings (V_{hold}, ∼−54 mV). Net currents were outward during the first half of the optical stimulus and inward during the second half.

Data are represented as mean ± SEM. See also Figure S8.

some evidence that they improve cortical information processing and thalamocortical communication through increased afferent synchrony (Cardin et al., 2009; Fries, 2009; Llinás et al., 1998; Siegle et al., 2014; Singer, 1993). The involvement of L6 CT circuits in gamma rhythms could be important for this improved processing, and the propensity of the L6 circuit to oscillate in the gamma range suggests that there is a local intra-L6 mechanism for synchronizing CT output.

The organization of inhibitory circuits in the thalamus is complex and varies across species and sensory pathways (Arcelli et al., 1997; Cox, 2014; Guillery and Harting, 2003; Wang et al., 2011). In most rodent thalamic nuclei (including VPm but not the visual thalamus), local GABAergic interneurons are virtually

absent. In other species, interneurons are found in many thalamic nuclei. Although interneurons receive direct excitatory input from the cortex, responses appear much weaker than those recorded in relay and TRN cells (Jurgens et al., 2012). Therefore, CT functions in pathways with interneurons might be more complex, but this is poorly understood.

The CT circuit mechanisms we describe here illustrate how simple differences in patterns of cortical activity can control the interactions between thalamic excitatory and inhibitory synapses and, therefore, bidirectionally regulate the flow of thalamocortical signals. Our work may also provide insight into how abnormalities in this circuit could lead to certain pathophysiological conditions (Huguenard and McCormick, 2007; Leresche

et al., 2012). The temporal pattern of CT activity is not the only factor determining CT effects; in vivo research has demonstrated important roles for topographic CT cell-thalamic cell alignment as well as the intrinsic physiological state of thalamic cells (Li and Ebner, 2007; Mease et al., 2014; Temereanca and Simons, 2004). Furthermore, intracortical mechanisms have also been shown to contribute strongly to the overall effects of L6 CT cells (Bortone et al., 2014; Kim et al., 2014; Olsen et al., 2012). Our work complements these elegant studies, and, together, they indicate that the dynamic states of the CT-relay cell and CT-TRN-relay cell synapses can exert fine-scale control of where, when, and how sensory signals are transferred to the cortex.

EXPERIMENTAL PROCEDURES

All procedures were carried out in accordance with the NIH Guidelines for the Care and Use of Laboratory Animals and were approved by the Brown University Institutional Animal Care and Use Committee.

Animals

This study is based on 61 transgenic mice heterozygous for *Ntsr1-Cre* (strain Tg(Ntsr1-cre)GN220Gsat/Mmucd). This strain expresses Cre recombinase in L6 CT projection cells (Bortone et al., 2014; Gong et al., 2007; Kim et al., 2014). All mice used had ICR genetic backgrounds (Charles River Laboratories). Of the 61 mice used here, 50 were bred by crossing *Ntsr1-Cre* males with wild-type ICR female mice. These mice were used for the majority of our experiments following viral induction of ChR2 in the somatosensory CT pathway (see below). The remaining mice were bred by crossing *Ntsr1-Cre* males with female mice homozygous for a conditional (Cre-dependent) ChR2-EYFP allele (Ai32 mice, The Jackson Laboratory, catalog no. 012569; n = 8 mice) or tdTomato allele (Ai9 mice, The Jackson Laboratory; n = 3 mice). The *Ntsr1/Ai32* mice were only used for the following experiments: low-frequency (0.1-Hz) optical CT stimulation studies with paired ML electrical stimulation or studies involving the electrical stimulation of TRN axons. All animals were group-housed, maintained on a 12:12-hr light-dark cycle, and provided food and water ad libitum.

Stereotactic Virus Injections

Adeno-associated virus carrying Cre-dependent genes for ChR2-EYFP fusion proteins was injected unilaterally into the barrel cortex of mice in vivo between postnatal days 11 and 14 (AAV2/1.Ef1a.DIO.hChRr2(H134R)-eYFP.WPRE.hGH, University of Pennsylvania Vector Core). Briefly, mice were anaesthetized with a Ketaset-Dexdormitor mixture diluted in sterile saline (Ketaset, 70 mg/kg; Dexdormitor, 0.25 mg/kg; intraperitoneally) and placed into a stereotaxic apparatus. A small craniotomy was made over the vibrissal region of S1, and a small volume of virus was delivered ($\sim$0.66 μl over 10-20 min; titer, 3.41 $\times$ 10^{12} genome copies/ml) by a glass micropipette attached to a Picospritzer pressure system (coordinates from the bregma for S1, 3.4 mm lateral; 0.80 posterior, 0.8–1.0 mm depth). The pipette was held in the final position for 10–15 min after injection before withdrawal from the brain. After surgery, mice were housed with a foster ICR mother with pups of similar age.

Slice Preparation

After allowing 8–12 days for ChR2 expression (between postnatal days 20 and 26), acute somatosensory thalamocortical or horizontal brain slices (300–350 μm thick) were prepared for in vitro recording, as described previously (Crandall et al., 2010; Cruikshank et al., 2010). Briefly, mice were anesthetized deeply with isoflurane before being decapitated. Brains were removed and placed in a cold ($\sim$4°C) oxygenated (95% O$_2$, 5% CO$_2$) slicing solution containing 3 mM KCl, 1.25 mM NaH$_2$PO$_4$, 10 mM MgSO$_4$, 0.5 mM CaCl$_2$, 26 mM NaHCO$_3$, 10 mM glucose, and 234 mM sucrose. Brain slices were cut using a vibrating tissue slicer (Leica VT1000) and then transferred to a holding chamber with warm (32°C) oxygenated artificial cerebrospinal fluid (ACSF) containing 126 mM NaCl, 3 mM KCl, 1.25 mM NaH$_2$PO$_4$, 2 mM MgSO$_4$, 2 mM CaCl$_2$, 26 mM NaHCO$_3$, and 10 mM glucose. After 20 min at 32°C, slices were then

stored at room temperature for a minimum of 1 hr in the same solution. In some cases the cortex, TRN, or VPm was removed from the slice using a scalpel.

In Vitro Recordings and Data Acquisition

For in vitro recordings, slices were transferred to a submersion recording chamber and bathed continually (2–3 ml/min) with warm (32°C) oxygenated (95% O$_2$, 5% CO$_2$) ACSF containing 126 mM NaCl, 3 mM KCl, 1.25 mM NaH$_2$PO$_4$, 1 mM MgSO$_4$, 1.2 mM CaCl$_2$, 26 mM NaHCO$_3$, and 10 mM glucose. Cells were visualized with infrared differential interference contrast microscopy and targeted by anatomical position. The majority of whole-cell recordings were obtained using patch pipettes containing the following potassium-based internal solution 130 mM K-gluconate, 4 mM KCl, 2 mM NaCl, 10 mM HEPES, 0.2 mM EGTA, 4 mM ATP-Mg, 0.3 mM guanosine triphosphate (GTP)-Tris, and 14 mM phosphocreatine-K (pH 7.25, $\sim$290 mOsm). For some voltage-clamp recordings, patch pipettes contained the following cesium-based internal solution: 130 mM Cs-gluconate, 4 mM CsCl, 2 mM NaCl, 10 mM HEPES, 0.2 mM EGTA, 4 mM ATP-Mg, 0.3 mM GTP-Tris, and 14 mM phosphocreatine-Tris (pH 7.25, $\sim$290 mOsm). All whole-cell recordings were corrected for a 14-mV liquid junction potential. Electrophysiological data were acquired and digitized at 20 kHz using Molecular Devices and Cambridge Electronic Design (CED) hardware and software. During whole-cell recordings, the pipette capacitances were neutralized, and series resistances (typically 10–25 MΩ) were compensated online (100% for current-clamp, 60%–80% for voltage-clamp). Signals were low pass-filtered at 10 kHz (current-clamp) or 3 kHz (voltage-clamp) prior to digitizing. Cell-attached recordings were obtained using patch-style pipettes filled with potassium-based internal solution (see above), and signals were high pass-filtered (100 Hz). The LFP was monitored with a patch-style pipette ($\sim$3 MΩ) filled with ACSF, and signals were band pass-filtered (1–200 Hz). The LFP pipette was placed in L5b. Pharmacological agents were prepared as recommended by the manufacturer and diluted in ACSF just before use. All pharmacological agents were bath-applied at least 10 min before subsequent experimental tests.

Optical and Electrical Stimulation

ChR2 was optically excited using a white light-emitting diode (LED) (cool white 5500K, Mightex) controlled by a Thorlabs LEDD1B driver. For most experiments, optical stimulation was directed at distal segments of CT axons within the thalamus with the light spot centered over the recorded postsynaptic thalamic cell. In those cases, collimated light (in 1-ms flashes) was reflected through a 40× water immersion objective, resulting in a spot diameter of $\sim$375 μm and a maximum LED power at the focal plane of 9.0 mW. For some experiments, the CT cell bodies were stimulated within cortical L6. In these experiments, collimated light was reflected through a 4× air objective, and the field diaphragm was adjusted to create a spot diameter of $\sim$250 μm (slightly larger than a barrel column). Under such conditions, the maximum LED power at the focal plane was 0.15 mW. These intracortical stimuli were applied in a ramp-like fashion. The intensities were increased gradually from near zero (0.0014 mW) to a peak value over the course of 1 s with approximately linear slopes. We refer to these stimuli as "light ramps." The peak intensities of the light ramps were adjusted for each experiment to obtain rhythmic cortical activity (in the gamma frequency range) with largely stable power for the duration of the stimulus, as described previously (Adesnik and Scanziani, 2010). Prior to the ramp stimulation, the cortex was initially mapped to find the L6 column that was best aligned with the recorded VPm cell (i.e., the L6 position at which 1-ms flash stimuli elicited maximal monosynaptic EPSPs in the recorded VPm cell). Extracellular electrical stimuli were delivered through paired microwires (25-μm diameter, 20–450 μA, 0.2-ms duration).

Dynamic Clamp

A full description of the dynamic clamp methods is presented in the Supplemental Experimental Procedures. Briefly, we applied simulated CT-evoked AMPAR-, NMDAR-, and GABA$_A$R-mediated conductances to VPm cells to test their respective roles in the modulation of excitability (Prinz et al., 2004) (CED Signal). Standard conductances were based on measurements of physiologically isolated AMPAR-, NMDAR-, and GABA$_A$R-mediated currents

(Figures 3 and 4). Current/voltage relationships, kinetics, and amplitudes of the simulated conductances were set to match the optically evoked CT responses. When the effects of the standard set of CT conductances on VPm spiking were determined, individual conductances were either removed or manipulated to test their roles in the modulation of VPm excitability.

Data Analysis

Analysis of electrophysiological data was performed in CED Signal 5, Molecular Devices Clampfit 10, AxoGraph X, and Microsoft Excel. Synaptic responses to optical or electrical stimulation were measured from postsynaptic neurons recorded in whole-cell current-clamp and voltage-clamp. The area or amplitude of an evoked EPSC/IPSC was measured from a baseline before the stimulus (0.2–10 ms depending on the frequency of the stimulation). The area of PSCs was measured over the 100 ms immediately after the onset of the stimulus for recordings using cesium solution and over the 10 ms immediately after the onset for recordings using potassium solutions. Values were based on average responses to 4–20 stimuli (typically 10). During high-frequency stimulation of TRN axons (Figure 5), stimulus artifacts were removed, and the dead time was replaced by a linear fit connecting the signal before and after. To calculate membrane variance, the voltage signals were band pass-filtered (1–200 Hz) to prevent contamination because of slow shifts in membrane potential and large amplitude spikes.

Statistical Analysis

Statistical comparisons were performed in OriginPro 8.0. Significance was assessed by using the appropriate parametric (paired t test) or non-parametric test (Mann-Whitney U test or Wilcoxon paired signed-rank test), as indicated in the Results. Data are represented as mean ± SEM, and statistical significance was defined as $p < 0.05$.

SUPPLEMENTAL INFORMATION

Supplemental Information includes eight figures and Supplemental Experimental Procedures and can be found with this article online at http://dx.doi.org/10.1016/j.neuron.2015.03.040.

REFERENCES

Adesnik, H., and Scanziani, M. (2010). Lateral competition for cortical space by layer-specific horizontal circuits. Nature *464*, 1155–1160.

Agmon, A., and Connors, B.W. (1991). Thalamocortical responses of mouse somatosensory (barrel) cortex in vitro. Neuroscience *41*, 365–379.

Alonso, J.M., Usrey, W.M., and Reid, R.C. (1996). Precisely correlated firing in cells of the lateral geniculate nucleus. Nature *383*, 815–819.

Arcelli, P., Frassoni, C., Regondi, M.C., De Biasi, S., and Spreafico, R. (1997). GABAergic neurons in mammalian thalamus: a marker of thalamic complexity? Brain Res. Bull. *42*, 27–37.

Augustinaite, S., Kuhn, B., Helm, P.J., and Heggelund, P. (2014). NMDA spike/plateau potentials in dendrites of thalamocortical neurons. J. Neurosci. *34*, 10892–10905.

Bastos, A.M., Briggs, F., Alitto, H.J., Mangun, G.R., and Usrey, W.M. (2014). Simultaneous recordings from the primary visual cortex and lateral geniculate nucleus reveal rhythmic interactions and a cortical source for γ-band oscillations. J. Neurosci. *34*, 7639–7644.

Beierlein, M., and Connors, B.W. (2002). Short-term dynamics of thalamocortical and intracortical synapses onto layer 6 neurons in neocortex. J. Neurophysiol. *88*, 1924–1932.

Bortone, D.S., Olsen, S.R., and Scanziani, M. (2014). Translaminar inhibitory cells recruited by layer 6 corticothalamic neurons suppress visual cortex. Neuron *82*, 474–485.

Bourassa, J., Pinault, D., and Deschênes, M. (1995). Corticothalamic projections from the cortical barrel field to the somatosensory thalamus in rats: a single-fibre study using biocytin as an anterograde tracer. Eur. J. Neurosci. *7*, 19–30.

Briggs, F., and Usrey, W.M. (2008). Emerging views of corticothalamic function. Curr. Opin. Neurobiol. *18*, 403–407.

Briggs, F., and Usrey, W.M. (2009a). Modulation of gamma-band activity across local cortical circuits. Front. Integr. Neurosci. *3*, 15.

Briggs, F., and Usrey, W.M. (2009b). Parallel processing in the corticogeniculate pathway of the macaque monkey. Neuron *62*, 135–146.

Bruno, R.M., and Sakmann, B. (2006). Cortex is driven by weak but synchronously active thalamocortical synapses. Science *312*, 1622–1627.

Cardin, J.A., Carlén, M., Meletis, K., Knoblich, U., Zhang, F., Deisseroth, K., Tsai, L.H., and Moore, C.I. (2009). Driving fast-spiking cells induces gamma rhythm and controls sensory responses. Nature *459*, 663–667.

Castro-Alamancos, M.A. (2002). Properties of primary sensory (lemniscal) synapses in the ventrobasal thalamus and the relay of high-frequency sensory inputs. J. Neurophysiol. *87*, 946–953.

Cox, C.L. (2014). Complex regulation of dendritic transmitter release from thalamic interneurons. Curr. Opin. Neurobiol. *29*, 126–132.

Cox, C.L., Huguenard, J.R., and Prince, D.A. (1997). Nucleus reticularis neurons mediate diverse inhibitory effects in thalamus. Proc. Natl. Acad. Sci. USA *94*, 8854–8859.

Crandall, S.R., Govindaiah, G., and Cox, C.L. (2010). Low-threshold Ca2+ current amplifies distal dendritic signaling in thalamic reticular neurons. J. Neurosci. *30*, 15419–15429.

Cruikshank, S.J., Lewis, T.J., and Connors, B.W. (2007). Synaptic basis for intense thalamocortical activation of feedforward inhibitory cells in neocortex. Nat. Neurosci. *10*, 462–468.

Cruikshank, S.J., Urabe, H., Nurmikko, A.V., and Connors, B.W. (2010). Pathway-specific feedforward circuits between thalamus and neocortex revealed by selective optical stimulation of axons. Neuron *65*, 230–245.

Crunelli, V., Lightowler, S., and Pollard, C.E. (1989). A T-type Ca2+ current underlies low-threshold Ca2+ potentials in cells of the cat and rat lateral geniculate nucleus. J. Physiol. *413*, 543–561.

Cudeiro, J., and Sillito, A.M. (2006). Looking back: corticothalamic feedback and early visual processing. Trends Neurosci. *29*, 298–306.

Deschênes, M., and Hu, B. (1990). Electrophysiology and pharmacology of the corticothalamic input to lateral thalamic nuclei: an intracellular study in the cat. Eur. J. Neurosci. *2*, 140–152.

Deschênes, M., Veinante, P., and Zhang, Z.W. (1998). The organization of corticothalamic projections: reciprocity versus parity. Brain Res. Brain Res. Rev. *28*, 286–308.

Diamond, M.E., Armstrong-James, M., Budway, M.J., and Ebner, F.F. (1992). Somatic sensory responses in the rostral sector of the posterior group (POm) and in the ventral posterior medial nucleus (VPM) of the rat thalamus: dependence on the barrel field cortex. J. Comp. Neurol. *319*, 66–84.

Diamond, M.E., von Heimendahl, M., Knutsen, P.M., Kleinfeld, D., and Ahissar, E. (2008). 'Where' and 'what' in the whisker sensorimotor system. Nat. Rev. Neurosci. *9*, 601–612.

Erişir, A., Van Horn, S.C., and Sherman, S.M. (1997). Relative numbers of cortical and brainstem inputs to the lateral geniculate nucleus. Proc. Natl. Acad. Sci. USA *94*, 1517–1520.

Ferster, D., and Lindström, S. (1985). Augmenting responses evoked in area 17 of the cat by intracortical axon collaterals of cortico-geniculate cells. J. Physiol. *367*, 217–232.

Fries, P. (2009). Neuronal gamma-band synchronization as a fundamental process in cortical computation. Annu. Rev. Neurosci. *32*, 209–224.

Ghosh, S., Murray, G.M., Turman, A.B., and Rowe, M.J. (1994). Corticothalamic influences on transmission of tactile information in the ventroposterolateral thalamus of the cat: effect of reversible inactivation of somatosensory cortical areas I and II. Exp. Brain Res. *100*, 276–286.

Golshani, P., Liu, X.B., and Jones, E.G. (2001). Differences in quantal amplitude reflect GluR4- subunit number at corticothalamic synapses on two populations of thalamic neurons. Proc. Natl. Acad. Sci. USA *98*, 4172–4177.

Gong, S., Doughty, M., Harbaugh, C.R., Cummins, A., Hatten, M.E., Heintz, N., and Gerfen, C.R. (2007). Targeting Cre recombinase to specific neuron populations with bacterial artificial chromosome constructs. J. Neurosci. *27*, 9817–9823.

Guido, W., and Weyand, T. (1995). Burst responses in thalamic relay cells of the awake behaving cat. J. Neurophysiol. *74*, 1782–1786.

Guillery, R.W., and Harting, J.K. (2003). Structure and connections of the thalamic reticular nucleus: advancing views over half a century. J. Comp. Neurol. *463*, 360–371.

Hirsch, J.C., Fourment, A., and Marc, M.E. (1983). Sleep-related variations of membrane potential in the lateral geniculate body relay neurons of the cat. Brain Res. *259*, 308–312.

Huguenard, J.R., and Prince, D.A. (1992). A novel T-type current underlies prolonged Ca(2+)-dependent burst firing in GABAergic neurons of rat thalamic reticular nucleus. J. Neurosci. *12*, 3804–3817.

Huguenard, J.R., and McCormick, D.A. (2007). Thalamic synchrony and dynamic regulation of global forebrain oscillations. Trends Neurosci. *30*, 350–356.

Huntsman, M.M., Porcello, D.M., Homanics, G.E., DeLorey, T.M., and Huguenard, J.R. (1999). Reciprocal inhibitory connections and network synchrony in the mammalian thalamus. Science *283*, 541–543.

Jahnsen, H., and Llinás, R. (1984). Electrophysiological properties of guinea-pig thalamic neurones: an in vitro study. J. Physiol. *349*, 205–226.

Jurgens, C.W., Bell, K.A., McQuiston, A.R., and Guido, W. (2012). Optogenetic stimulation of the corticothalamic pathway affects relay cells and GABAergic neurons differently in the mouse visual thalamus. PLoS ONE *7*, e45717.

Kao, C.Q., and Coulter, D.A. (1997). Physiology and pharmacology of corticothalamic stimulation-evoked responses in rat somatosensory thalamic neurons in vitro. J. Neurophysiol. *77*, 2661–2676.

Kim, U., Sanchez-Vives, M.V., and McCormick, D.A. (1997). Functional dynamics of GABAergic inhibition in the thalamus. Science *278*, 130–134.

Kim, J., Matney, C.J., Blankenship, A., Hestrin, S., and Brown, S.P. (2014). Layer 6 corticothalamic neurons activate a cortical output layer, layer 5a. J. Neurosci. *34*, 9656–9664.

Kwegyir-Afful, E.E., and Simons, D.J. (2009). Subthreshold receptive field properties distinguish different classes of corticothalamic neurons in the somatosensory system. J. Neurosci. *29*, 964–972.

Lam, Y.W., and Sherman, S.M. (2010). Functional organization of the somatosensory cortical layer 6 feedback to the thalamus. Cereb. Cortex *20*, 13–24.

Landisman, C.E., and Connors, B.W. (2007). VPM and PoM nuclei of the rat somatosensory thalamus: intrinsic neuronal properties and corticothalamic feedback. Cereb. Cortex *17*, 2853–2865.

Landisman, C.E., Long, M.A., Beierlein, M., Deans, M.R., Paul, D.L., and Connors, B.W. (2002). Electrical synapses in the thalamic reticular nucleus. J. Neurosci. *22*, 1002–1009.

Landry, P., and Dykes, R.W. (1985). Identification of two populations of corticothalamic neurons in cat primary somatosensory cortex. Exp. Brain Res. *60*, 289–298.

Lee, S., Carvell, G.E., and Simons, D.J. (2008). Motor modulation of afferent somatosensory circuits. Nat. Neurosci. *11*, 1430–1438.

Leresche, N., Lambert, R.C., Errington, A.C., and Crunelli, V. (2012). From sleep spindles of natural sleep to spike and wave discharges of typical absence seizures: is the hypothesis still valid? Pflugers Arch. *463*, 201–212.

Li, L., and Ebner, F.F. (2007). Cortical modulation of spatial and angular tuning maps in the rat thalamus. J. Neurosci. *27*, 167–179.

Liu, X.B., Honda, C.N., and Jones, E.G. (1995). Distribution of four types of synapse on physiologically identified relay neurons in the ventral posterior thalamic nucleus of the cat. J. Comp. Neurol. *352*, 69–91.

Llinás, R., Ribary, U., Contreras, D., and Pedroarena, C. (1998). The neuronal basis for consciousness. Philos. Trans. R. Soc. Lond. B Biol. Sci. *353*, 1841–1849.

MacDermott, A.B., and Dale, N. (1987). Receptors, ion channels and synaptic potentials underlying the integrative actions of excitatory amino acids. Trends Neurosci. *10*, 280–284.

Mayer, M.L., Westbrook, G.L., and Guthrie, P.B. (1984). Voltage-dependent block by Mg2+ of NMDA responses in spinal cord neurones. Nature *309*, 261–263.

McAlonan, K., Cavanaugh, J., and Wurtz, R.H. (2008). Guarding the gateway to cortex with attention in visual thalamus. Nature *456*, 391–394.

McCormick, D.A., and Feeser, H.R. (1990). Functional implications of burst firing and single spike activity in lateral geniculate relay neurons. Neuroscience *39*, 103–113.

Mease, R.A., Krieger, P., and Groh, A. (2014). Cortical control of adaptation and sensory relay mode in the thalamus. Proc. Natl. Acad. Sci. USA *111*, 6798–6803.

Miyata, M. (2007). Distinct properties of corticothalamic and primary sensory synapses to thalamic neurons. Neurosci. Res. *59*, 377–382.

Normand, E.A., Crandall, S.R., Thorn, C.A., Murphy, E.M., Voelcker, B., Browning, C., Machan, J.T., Moore, C.I., Connors, B.W., and Zervas, M. (2013). Temporal and mosaic Tsc1 deletion in the developing thalamus disrupts thalamocortical circuitry, neural function, and behavior. Neuron *78*, 895–909.

Nowak, L., Bregestovski, P., Ascher, P., Herbet, A., and Prochiantz, A. (1984). Magnesium gates glutamate-activated channels in mouse central neurones. Nature *307*, 462–465.

O'Connor, D.H., Fukui, M.M., Pinsk, M.A., and Kastner, S. (2002). Attention modulates responses in the human lateral geniculate nucleus. Nat. Neurosci. *5*, 1203–1209.

O'Connor, D.H., Peron, S.P., Huber, D., and Svoboda, K. (2010). Neural activity in barrel cortex underlying vibrissa-based object localization in mice. Neuron *67*, 1048–1061.

Olsen, S.R., Bortone, D.S., Adesnik, H., and Scanziani, M. (2012). Gain control by layer six in cortical circuits of vision. Nature *483*, 47–52.

Paz, J.T., Bryant, A.S., Peng, K., Fenno, L., Yizhar, O., Frankel, W.N., Deisseroth, K., and Huguenard, J.R. (2011). A new mode of corticothalamic transmission revealed in the Gria4(-/-) model of absence epilepsy. Nat. Neurosci. *14*, 1167–1173.

Pedroarena, C.M., and Llinás, R. (2001). Interactions of synaptic and intrinsic electroresponsiveness determine corticothalamic activation dynamics. Thalamus Relat. Syst. *1*, 3–14.

Prinz, A.A., Abbott, L.F., and Marder, E. (2004). The dynamic clamp comes of age. Trends Neurosci. *27*, 218–224.

Scharfman, H.E., Lu, S.M., Guido, W., Adams, P.R., and Sherman, S.M. (1990). N-methyl-D-aspartate receptors contribute to excitatory postsynaptic

potentials of cat lateral geniculate neurons recorded in thalamic slices. Proc. Natl. Acad. Sci. USA *87*, 4548–4552.

Sherman, S.M., and Koch, C. (1986). The control of retinogeniculate transmission in the mammalian lateral geniculate nucleus. Exp. Brain Res. *63*, 1–20.

Siegle, J.H., Pritchett, D.L., and Moore, C.I. (2014). Gamma-range synchronization of fast-spiking interneurons can enhance detection of tactile stimuli. Nat. Neurosci. *17*, 1371–1379.

Sillito, A.M., Jones, H.E., Gerstein, G.L., and West, D.C. (1994). Feature-linked synchronization of thalamic relay cell firing induced by feedback from the visual cortex. Nature *369*, 479–482.

Singer, W. (1993). Synchronization of cortical activity and its putative role in information processing and learning. Annu. Rev. Physiol. *55*, 349–374.

Steriade, M., McCormick, D.A., and Sejnowski, T.J. (1993). Thalamocortical oscillations in the sleeping and aroused brain. Science *262*, 679–685.

Steriade, M., Contreras, D., Amzica, F., and Timofeev, I. (1996). Synchronization of fast (30–40 Hz) spontaneous oscillations in intrathalamic and thalamocortical networks. J. Neurosci. *16*, 2788–2808.

Sun, Y.G., and Beierlein, M. (2011). Receptor saturation controls short-term synaptic plasticity at corticothalamic synapses. J. Neurophysiol. *105*, 2319–2329.

Swadlow, H.A. (1989). Efferent neurons and suspected interneurons in S-1 vibrissa cortex of the awake rabbit: receptive fields and axonal properties. J. Neurophysiol. *62*, 288–308.

Swadlow, H.A., and Weyand, T.G. (1987). Corticogeniculate neurons, corticotectal neurons, and suspected interneurons in visual cortex of awake rabbits: receptive-field properties, axonal properties, and effects of EEG arousal. J. Neurophysiol. *57*, 977–1001.

Swadlow, H.A., and Gusev, A.G. (2001). The impact of 'bursting' thalamic impulses at a neocortical synapse. Nat. Neurosci. *4*, 402–408.

Temereanca, S., and Simons, D.J. (2004). Functional topography of corticothalamic feedback enhances thalamic spatial response tuning in the somatosensory whisker/barrel system. Neuron *41*, 639–651.

Turner, J.P., and Salt, T.E. (1998). Characterization of sensory and corticothalamic excitatory inputs to rat thalamocortical neurones in vitro. J. Physiol. *510*, 829–843.

Usrey, W.M., Alonso, J.M., and Reid, R.C. (2000). Synaptic interactions between thalamic inputs to simple cells in cat visual cortex. J. Neurosci. *20*, 5461–5467.

Van Horn, S.C., Erişir, A., and Sherman, S.M. (2000). Relative distribution of synapses in the A-laminae of the lateral geniculate nucleus of the cat. J. Comp. Neurol. *416*, 509–520.

von Krosigk, M., Monckton, J.E., Reiner, P.B., and McCormick, D.A. (1999). Dynamic properties of corticothalamic excitatory postsynaptic potentials and thalamic reticular inhibitory postsynaptic potentials in thalamocortical neurons of the guinea-pig dorsal lateral geniculate nucleus. Neuroscience *91*, 7–20.

Wang, X., Sommer, F.T., and Hirsch, J.A. (2011). Inhibitory circuits for visual processing in thalamus. Curr. Opin. Neurobiol. *21*, 726–733.

Yang, Q., Chen, C.C., Ramos, R.L., Katz, E., Keller, A., and Brumberg, J.C. (2014). Intrinsic properties of and thalamocortical inputs onto identified corticothalamic-VPM neurons. Somatosens. Mot. Res. *31*, 78–93.

Yuan, B., Morrow, T.J., and Casey, K.L. (1986). Corticofugal influences of S1 cortex on ventrobasal thalamic neurons in the awake rat. J. Neurosci. *6*, 3611–3617.

Zhou, Y., Liu, B.H., Wu, G.K., Kim, Y.J., Xiao, Z., Tao, H.W., and Zhang, L.I. (2010). Preceding inhibition silences layer 6 neurons in auditory cortex. Neuron *65*, 706–717.

Zucker, R.S., and Regehr, W.G. (2002). Short-term synaptic plasticity. Annu. Rev. Physiol. *64*, 355–405.